Influence of Sensor Coating and Topography on Protein and Nanoparticle Interaction with Supported Lipid Bilayers

Hui Yin, Arielle C. Mensch, Christian A. Lochbaum, Isabel U. Foreman-Ortiz, Emily R. Caudill, Robert J. Hamers, Joel A. Pedersen*

ABSTRACT: Supported lipid bilayers have proven valuable model systems for studying interactions of proteins, peptides, and nanoparticles with biological membranes. The physicochemical properties (e.g., topography, coating) of the solid substrate may affect the formation and properties of supported phospholipid bilayers and thus subsequent interactions with biomolecules or nanoparticles. Here, we examine the influence of support coating (SiO_2 vs. Si_3N_4) and topography (sensors with embedded vs. protruding gold nanodisks for nanoplasmonic sensing) on the formation and subsequent interactions of supported phospholipid bilayers with the model protein cytochrome *c* and with cationic polymer-wrapped quantum dots using quartz crystal microbalance with dissipation monitoring and nanoplasmonic sensing. The specific protein and nanoparticle were chosen because they differ in the degree to which they penetrate the bilayer. We find that bilayer formation and subsequent non-penetrative association with cytochrome *c* was not significantly influenced by substrate composition or topography. In contrast, the interactions of the nanoparticles with supported lipid bilayers depended on substrate composition. We attribute the substrate-dependence nanoparticle adsorption to the more negative zeta-potential above silica-supported than silicon nitride-supported bilayers and the penetration of the cationic polymer wrapping the nanoparticles into the bilayer. Our results indicate that the degree to which nanoscale analytes interact with supported lipid bilayers may be influenced by the underlying substrate material.

KEYWORDS: quartz crystal microbalance with dissipation monitoring (QCM-D), nanoplasmonic sensing (NPS), localized surface plasmon resonance (LSPR), streaming current, supported lipid bilayer (SLB), cytochrome *c*

INTRODUCTION

Solid-supported lipid bilayers (SLBs) are widely used as model systems to understand interactions between cellular membranes and a variety of analytes including plant secondary metabolites, organic contaminants, peptides, proteins, viruses, and nanoparticles.[1–10] Supported lipid bilayers are frequently formed on oxide-coated sensors used in surface-sensitive techniques such as quartz crystal microbalance with dissipation monitoring (QCM-D), ellipsometry, optical waveguide lightmode spectroscopy, multi-parametric surface plasmon resonance, localized surface plasmon resonance (LSPR) sensing (nanoplasmonic sensing, NPS), and dual polarization interferometry.[6,11–19] The sensors employed by these surface-sensitive techniques can differ in coating material or architecture. The composition of the oxide coating can impact phospholipid bilayer formation and the distances between SLB and the sensor surfaces.[20–22] For example, zwitterionic egg-yolk phosphatidylcholine vesicles adsorbed intact onto TiO_2-, oxidized Pt-, and Au-coated sensors and did not form a bilayer.[20] In contrast, absorption onto either SiO_2- or Si_3N_4-coated sensors proceeded until a critical surface coverage was attained and the adsorbed vesicles spontaneously fused and ruptured to form an SLB.[20] The distance between SLBs composed of zwitterionic 1,2-dioleoyl-*sn*-glycero-3-phosphocholine (DOPC) and oxide surfaces is larger for TiO_2- than for SiO_2-coated sensors.[21] Incorporation of cationic lipids into supported DOPC bilayers decreases SLB-oxide distance on TiO_2 surfaces, but does not affect the separation distance of those on SiO_2 surfaces.[21] The distal leaflet of SLBs formed with mixtures of zwitterionic phosphatidylcholine and cationic phosphatidylserine lipids on oxidized mica is depleted in cationic

lipids when compared to those formed on SiO_2.[22] Silica and silicon nitride are commonly used coatings for forming SLBs on QCM-D and NPS sensors, respectively.[23] These materials differ in basic physical and chemical properties including refractive indices (1.47 vs. 2.00), isoelectric points (2-3.5 vs. 3-9, depending upon the relative site density of amphoteric silanol and amine groups),[24–26] Knoop hardness (12 vs. 15),[27] and Hamaker constant (1.6×10^{-21} J vs. 45×10^{-21} J).[28] The extent to which the composition of the substrate underlying supported lipid bilayers affects interactions of analytes with such model membranes has received little study.

The surface-sensitive techniques mentioned above employ sensors with different architectures, which in some cases leads to topographies that are not planar. Topographical differences between planar and non-planar sensor surfaces may alter the rates or extent of SLB formation or analyte interaction. For example, protein adsorption to planar SiO_2 differs from that to pyrolytic carbon with nanoscale surface roughness as measured by radioimmunoassay and ellipsometry.[29] Optical waveguide light spectroscopy requires diffraction gratings etched into sensor surfaces which creates surface height changes on the order of 10 nm laterally along the sensor surface.[30] Nanoplasmonic sensing architectures include nanoparticles deposited on or embedded in sensor surfaces,[31–33] nanoscale holes, and nanoscale wells.[21,34] Sensors topography may influence the measurement sensitivity and the kinetics and extent of interactions of biomolecules and nanoparticles.

Integration of QCM-D and NPS allows simultaneous acquisition of complementary acoustic and optical information using a single sensor.[4,35] Quartz crystal microbalance with dissipation monitoring detects both adsorbates and dynamically coupled solvent while NPS measures analytes (but not solvent) in close proximity to the sensor surface (e.g., 10-30 nm).[4,36–38] Sensors compatible with both techniques have noble metal nanoparticles deposited onto SiO_2- or

Si_3N_4-coated sensors.[39] The frequency of maximum plasmon absorption (λ_{max}) of NPS sensors depends on the optical properties of nanoparticles, dielectric materials, and nanoparticle geometry used,[13,31,33,39–44] leading to an array of sensor coating and topography combinations. Silver nanotriangles exhibit larger hexadecanethiol-induced shift in λ_{max} than do gold nanotriangles,[31] refractive index sensitivity of rod-like Ag nanoparticles is ~1.2 times that of triangular nanoparticles and ~1.5 times that of spherical ones,[32] and measurement sensitivity of bare gold nanodisks is higher than those of the SiO_2- or TiO_2-coated substrates by a factor of more than two.[33] Metal oxide topography influences measurement sensitivity and analyte interactions: sensors with Au nanodisks embedded and coated with SiO_2 such that the exposed sensor surface is flat exhibit lower bulk refractive index sensitivity (attributable to the average dielectric constant of the medium in contact with the gold), ~10% higher maximal vesicle rupture rate, and higher Avidin adsorption rate than sensors with protruding Au nanodisks coated with SiO_2.[45] Given development of combined QCM-D and NPS as a promising tool for monitoring SLBs, as well as other techniques involving topographically varied sensors, the effect of nanoscale topography on SLB formation and subsequent analyte interaction warrants study.

Here, we evaluate the extent to which substrate composition (for negatively charged SiO_2- and Si_3N_4-coated sensors) and topography (for flat and protruding Au nanodisks deposited in NPS sensors) impact SLB formation and subsequent protein or nanoparticle interaction. We compared SiO_2- and Si_3N_4-sensor coatings using both QCM-D and streaming current measurements to examine the influence of coating on SLB formation and subsequent interaction with cytochrome *c* or cationic polymer-wrapped quantum dots (QDs). We chose cytochrome *c* and cationic polymer-wrapped QDs because prior work indicated they differ in the degree they penetrate supported zwitterionic lipid bilayers.[9,46,47] We used combined QCM-D and NPS to compare the formation of

SLBs and subsequent adsorption of either cytochrome *c* or QDs on topographically protruding and flat Au nanodisk sensors coated with Si_3N_4.

MATERIALS AND METHODS

Materials. Phospholipids were purchased from Avanti Polar Lipids: 1,2-dioleoyl-*sn*-glycero-3-phosphocholine (DOPC), 1′,3′-bis[1,2-dioleoyl-*sn*-glycero-3-phospho]-*sn*-glycerol (18:1 cardiolipin, TOCL), and plant-derived cholesterol (Chol; 700100P). Sphingomyelin (SM) derived from chicken egg yolk (S0756) and equine heart cytochrome *c* (M_r =12,384) were obtained from Sigma-Aldrich. We procured 2-[4-(2-hydroxyethyl)piperazin-1-yl] ethanesulfonic acid (HEPES), NaCl, and $CaCl_2 \cdot 2H_2O$ from Fisher Scientific. Cadmium selenide quantum dots (QDs) with zinc sulfide shells and wrapped in poly(diallyldimethylammonium chloride) (PDDA; M_r = 200,000) were purchased from OceanNanotech (PDDA-QDs; QSQ-620). The manufacturer reported the core size to be 3.3 nm, shell thickness to be 2.5 nm, and PDDA layer thickness to be ~2 nm. All materials were used as received. All aqueous solutions were prepared in ultrapure water (18.2 MΩ·cm, Barnstead Nanopure) and, unless otherwise noted, were buffered to pH 7.4 with 0.01 M HEPES.

Cytochrome *c* was gently dissolved in 0.01 M NaCl to a stock concentration of 5 mg·mL^{-1}. The cytochrome *c* stock solution was evenly divided into several microcentrifuge tubes and stored at −20 °C. Once thawed the cytochrome *c* solution was used within 1 week.

Preparation and Characterization of Small Unilamellar Vesicles. Small unilamellar vesicles composed of DOPC, a 91.2:8.8 molar ratio of DOPC and TOCL, or 3:1:1 molar ratio of DOPC, SM, and Chol were formed by the extrusion method.[6,48] Briefly, dry lipids were dissolved in chloroform to concentrations of 5 mg·mL^{-1} for DOPC and TOCL or 1 mg·mL^{-1} for Chol and SM. Components were mixed to their desired ratios as needed in a glass vial and mixed. Chloroform was evaporated under a gentle stream of ultrapure N_2 gas. The dried lipid films were held under vacuum for at least 1 h to remove any residual chloroform. The lipids were rehydrated in 0.001 M NaCl to a stock concentration of 2.5 mg·mL^{-1} for DOPC and 91.2:8.8 mol.% DOPC:TOCL or 1.25 mg·mL^{-1} for 60:20:20 mol% DOPC:SM:Chol. (Bilayer

compositions are given in mol% throughout.) Lipid suspensions were sequentially sonicated for 30 min vortexed for 30 s, sonicated for 5 min, and vortexed for 10 s. Lipids were transferred into a 2 mL polypropylene tube and subjected to three freeze/thaw cycles (liquid N_2, 3 min/bath sonicator, 5 min). After 10 s vortexing, the lipids were extruded 11 times through 50 nm polycarbonate membranes (Avanti Polar Lipids, 610003) with an extruder set (Avanti Polar Lipids, 610 000). The hydrodynamic diameter (d_h) and zeta-potential (ζ) of the small unilamellar vesicles were determined by dynamic light scattering and laser Doppler microelectrophoresis (Malvern Zetasizer Nano ZS), and are reported in Table S1. The unilamellar vesicles were stored at 4 °C and used within one week.

Quartz Crystal Microbalance with Dissipation Monitoring (QCM-D). Formation of SLBs and subsequent interaction of cytochrome *c* or PDDA-QDs were monitored with QCM-D. In QCM-D, an AC voltage imposed across a piezoelectric AT-cut quartz crystal drives oscillations in the shear mode at a resonant frequency. QCM-D measures changes in the resonant frequency (Δf) and energy dissipation (ΔD) induced by the interaction of an analyte with the sensor surface. Frequency shifts reflect changes in mass coupled to the sensor surface and include both the mass of the analyte and that of any dynamically coupled solvent. Changes in the energy dissipation factor are related to the viscoelastic properties of laterally homogeneous adlayers and the stiffness of particle-surface contacts for adlayers composed of discrete nanosized objects.[49–51]

For a rigidly coupled adlayer (defined as $\Delta D_\nu/(-\Delta f_\nu/\nu) << 4 \times 10^{-7}$ Hz^{-1}, where ν is the harmonic number),[50] the frequency shift can be related to the acoustic surface mass density ($\Gamma_{QCM\text{-}D}$) via the Sauerbrey relationship:[52]

$$\Gamma_{QCM\text{-}D} = -C\frac{\Delta f_\nu}{\nu} \quad (1)$$

where C is the mass sensitivity constant (18 ng·cm^{-2}·Hz^{-1} at the fundamental frequency, f_1 = 4.95 MHz) that depends on the fundamental resonance frequency and the properties of the quartz crystal. For more dissipative laterally homogeneous adlayers, the acoustic surface mass density is related to the change in frequency and the adlayer viscoelastic properties:[50,53,54]

$$\Gamma_{\text{QCM-D}} \approx -C\frac{\Delta f_\nu}{\nu}\left(1-\nu\omega_1\rho_l\eta_l\frac{G_f''}{\rho_f\left(G_f'^2+G_f''^2\right)}\right)^{-1} \quad (2)$$

in which the *l* and *f* subscripts refer to the liquid and the film, ρ is density, $\omega_1 = 2\pi f_1$, η is dynamic viscosity, G' is the storage modulus, and G'' is the loss modulus.

Quartz crystal microbalance experiments were conducted using a Q-Sense E4 system (Biolin Scientific, Göteborg, Sweden) at 25 °C using four temperature-controlled, liquid flow cells (QFM 401) except for the subset of experiments in which simultaneous nanoplasmonic sensing measurements were made (*vide infra*). The QCM-D sensors acquired from Biolin Scientific were manufactured by sputter-coating (SC) with either Si_3N_4 (QSX328) or SiO_2 (QSX303); reference sensors coated with Si_3N_4 via plasma-enhanced chemical vapor deposition (PECVD; ACO-REF1) were obtained from Insplorion (Göteborg, Sweden). Schematics of the coatings on these sensors are shown in Figure 1. Prior to use, sensors were exposed to UV/Ozone for 15 min (Bioforce Nanosciences UV/Ozone Procleaner).

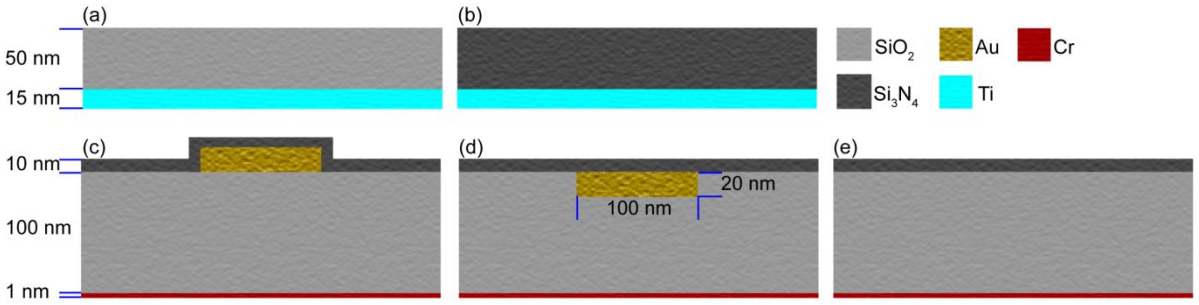

Figure 1. Schematic illustration of the sensors used in the QCM-D and NPS experiments. QCM-D sensors were coated with (a) SiO_2 or (b) Si_3N_4. NPS sensors incorporated 100 nm diameter nanoplasmonic gold disks that either (c) protruded from or (d) were embedded in the SiO_2 layer. (e) Reference NPS sensors lacked nanoplasmonic disks. All NPS sensors were coated with 10 nm of Si_3N_4. Layer thicknesses and gold disk dimensions are to scale. The SiO_2 and Si_3N_4 layers on the QCM-D sensors were deposited by sputter coating; the Si_3N_4 layers on the NPS sensors were formed via PECVD.

After mounting sensors into the flow cells, supported lipid bilayers were formed by the vesicle fusion method.[48] After flowing ultrapure water (unbuffered) and a solution of 0.15 M NaCl (with 0.005 M $CaCl_2$ in the case of bilayers containing TOCL) at a rate of 0.1 mL·min^{-1} sequentially (until a stable baseline signal was obtained, as determined by $df_5/dt < 0.05$ Hz·min^{-1}), a vesicle suspension (composition below) flowed over the sensor until a supported lipid bilayer formed. During this time a minimum in Δf and a maximum in ΔD were reached (signaling attainment of a critical surface concentration of adsorbed vesicles), followed by a rise in Δf and a decrease in ΔD (reflecting the commencement of vesicle rupture and release of the solution inside the vesicles), and the attainment of stable plateau values of both consistent with the formation of a supported lipid bilayer.[55] The 91.2:8.8% DOPC:TOCL vesicles were introduced in 0.15 M NaCl with 0.005 M $CaCl_2$ and at a concentration of 0.125 mg·mL^{-1}; DOPC and 60:20:20% DOPC/SM/Chol vesicles were introduced at 0.03125 mg·mL^{-1} in 0.15 M NaCl. After formation, the bilayers were rinsed with either 0.15 M NaCl with 0.005 M $CaCl_2$ (91.2:8.8% DOPC+TOCL bilayers) or 0.15 M NaCl (DOPC and 60:20:20% DOPC/SM/Chol bilayers), followed by sequential rises with 0.15 M NaCl and 0.01 M NaCl to remove any adhering vesicles. For experiments with cytochrome *c*, the flow rate was reduced to 0.05 mL·min^{-1} and 0.05 mg·mL^{-1} cytochrome *c* solution diluted in 0.01 M NaCl flowed for 30 min and then the flow was halted for 30 min. As previously reported, flow was halted to increase time for cytochrome *c* interaction with the bilayer.[9] After this period, the flow rate was increased to 0.1 mL·min^{-1} and 0.01 M NaCl was flowed to remove any weakly adsorbed protein. For experiments with PDDA-QDs, 1 nM (number concentration) of PDDA-QDs in 0.01 M NaCl was flowed over the bilayers for 20 min prior to rinsing with PDDA-QD-free buffer. The length of each rinsing period was dictated by the time needed for attainment of stable Δf and ΔD values. The initial attachment rate, r_d, of cytochrome *c* or PDDA-QDs attached onto the indicated SLBs was calculated for the first 30 s of attachment. Each experiment was performed in triplicate. Data comparisons were made using *t*-tests with Welch's correction or one-way ANOVA with a Tukey *post hoc* test at the $\alpha = 0.05$ level of significance.

After the experiments, the temperature in the QCM-D cells was raised to 40 °C and a 2% solution of sodium dodecyl sulfate (SDS) was flowed over the sensors (0.35 mL·min^{-1}, 15 min). The sensors were

removed, used gold-coated QCM-D crystals were mounted in the flow cells, and the flow cells were sequentially rinsed with 2% Hellmanex, Cobas solution, and water (20 min for each solution). The Si_3N_4- or SiO_2-coated sensors were immersed in 2% SDS solution for 20 min before extensive rinsing with ultrapure water, ethanol, and ultrapure water before drying with N_2.

Nanoplasmonic Sensing. Nanoplasmonic sensing is an optical method based on the excitation of metallic nanostructures by light and has a detection length of 10-30 nm.[4,36–38] The conduction electrons of the metallic nanostructures couple with the field oscillations of electromagnetic waves. This coupling is strongest at specific resonance energies, resulting in extinction at characteristic wavelengths in the optical spectrum. The wavelength of maximum extinction (λ_{max}) corresponds to the plasmon resonance frequency and exhibits high sensitivity to the refractive index at the interface of the nanostructure. In the instrumental configuration used here, white light was delivered to the top of the flow chamber via a fiber optic cable and the reflected intensity was monitored as a function of wavelength. The Acoulyte NPS module (Insplorion AB, Göteborg, Sweden) interfaces with the QSense window module (QWM401) to allow simultaneous acquisition of NPS and QCM-D data.

For these experiments, gold-coated QSense sensors modified with a 100 nm SiO_2 spacer layer and equipped with gold nanoplasmonic disks were used. Gold nanoplasmonic disks had diameters of 100 nm and heights of 20 nm and were spaced ~100 nm apart (thus covering 10-12%) of the surface. We employed nanoplasmonic disk-decorated QCM-D sensors in two distinct topographies: flat, with the Au disks embedded in the SiO_2 layer (ACO-FLT1, Insplorion) and with the Au disks placed atop the SiO_2 layer and protruding above the plane formed by this layer (ACO-SEN1, Insplorion) as illustrated in Figure 1. The nanoplasmonic disks were coated with a 10 nm layer of Si_3N_4 by PECVD. The surface area of the sensor with protruding nanoplasmonic disks was larger than the flat sensors by a factor of 1.1. Procedures for pretreating sensors, supported lipid bilayer formation, and cytochrome *c* adsorption experiments were as described in the section on QCM-D. After completion of experiments, the Acoulyte sensors were replaced with Au-coated sensors and the window cell was cleaned as described in the previous section. Acoulyte

sensors were immersed in 2% SDS solution (20 min), extensively rinsed sequentially with ultrapure water and ethanol alternatively, and dried under N_2 flow.

The bulk refractive index sensitivities of the Acoulyte sensors were determined as described previously.[4,9,56] Briefly, after a stable baseline was obtained by flowing ultrapure water (no buffer) over an Acoulyte sensor mounted in the window cell, solutions of increasing glycerol concentrations (5-35 wt% at 4 wt% increments) were flowed. Thereafter, ultrapure water (no buffer) and 0.15 M NaCl were sequentially flowed over the sensor until stable baselines were obtained, and 0.125 mg·mL^{-1} DOPC vesicles in 0.15 M NaCl were flowed across the sensor until a supported lipid bilayer was formed. After rinsing the supported DOPC bilayer sequentially with 0.15 M NaCl and ultrapure water (no buffer), glycerol solutions were flowed over the bilayer as described above. The flow rate was 100 μL·min^{-1}, and the temperature was maintained at 25 °C. Duplicate determinations of bulk refractive index sensitivity were conducted, and average values are reported. The refractive indices of the solutions used were independently measured at 633 nm using a Rudolph Research J157 Automatic Refractometer in triplicate.

The optical mass was calculated from $\Delta\lambda_{max}$ as previously described.[4,9,56] Vesicle adsorption/rupture rates (r) were obtained by taking the first derivative of the raw $\Delta\lambda$ with respect to time:

$$r = \frac{d\Delta\lambda}{dt} \qquad (3)$$

The first derivative curve was then smoothed by using Savitzky-Golay function (polynomial order = 2, points in window = 50).

Simulations of Nanoplasmonic Sensors. Simulations of nanoplasmonic sensor responses were performed using Comsol Multiphysics 5.5 Wave Optics module in a fully three-dimensional geometry. Floquet periodic boundary conditions were used to simulate two-dimensional arrays of gold nanodisks with dimensions equal to those used in the experiment (100 nm diameter, 20 nm thick, on a 200 nm repeat period). Planar and protruding geometries were used. Full-field electromagnetic simulations were performed as a function of wavelength to determine the optical characteristics of sensor arrays, and the

reflectivity, transmission, and absorption were determined at each wavelength. Wavelength-dependent optical constants (*n* and *k*) of gold, SiO_2, and Si_3N_4 were taken from literature sources.[57–59]

Streaming Current Measurements. Streaming an aqueous solution through a capillary system generates an electrical response (the streaming potential or the streaming current). This response can be continuously monitored with increasing pressure difference. For flat samples in a rectangular slit streaming channel, the electrokinetic phenomenon of the streaming current (I_{str}) can be used to calculate ζ according to the Helmholtz-Smoluchowski equation:[60]

$$\zeta = \frac{\eta}{\varepsilon_r \varepsilon_0} \cdot \frac{dI_{str}}{dp} \cdot \frac{L}{bh} \qquad (4)$$

where η is solution dynamic viscosity, ε_r is the relative permittivity, ε_0 is the permittivity of vacuum, p is pressure, L is the length of the rectangular slit channel, b is channel width, and h is channel height.

Streaming current was measured using Anton Paar SurPASS™ 3 instrument with an adjustable gap cell for planar samples 10 mm × 20 mm. We determined ζ for SiO_2 and Si_3N_4 surfaces using respectively a silicon wafer having a 30 nm thermal oxide layer (Universitywafer, Massachusetts, USA) and Si wafers coated with a 10 nm Si_3N_4 layer by PECVD on the thermal oxide layer. Before streaming current measurement, wafers were cleaned for 30 min using a 1:1:5 volume ratio of aqueous solutions of NH_4OH (28.0-30.0%, ElectroPUR™ SEMI), H_2O_2 (35 wt.%, Acrōs Organics), and ultrapure water (no buffer) at 70 °C. The wafers were extensively rinsed with ultrapure water (no buffer) under sonication, treated for 15 min by UV/Ozone, and immediately loaded into the measurement cell. Streaming current was measured for the bare SiO_2- and Si_3N_4-coated wafers in 0.01 M NaCl. We then formed supported lipid bilayers on the wafer surface and measured the streaming current of the solid-supported phospholipid bilayers. The DOPC and 91.2:8.8% DOPC:TOCL vesicles were prepared with the vesicle extrusion method as described above, except that the lipid was hydrated in 0.01 M NaCl, 0.005 M $CaCl_2$ solution at pH 4 and extruded 31 times through the polycarbonate membrane. Briefly, 80 mL of a 0.2 mg·mL^{-1} DOPC or 91.2:8.8% DOPC:TOCL vesicle suspension in 0.001 M NaCl was injected into the measurement cell followed by rinsing 10 times with an equivalent volume of vesicle-free solution (~40 min) to form a bilayer on the wafer. After

incubating the bilayers for 2 h, the cell was rinsed 10 times with 200 mL of 0.01 M NaCl. The streaming current of the bilayer formed was measured in the same electrolyte.[61,62] For each sample (either the wafer or the bilayer formed on the wafer), I_{str} was measured four times under continuous N_2 purging.

RESULTS AND DISCUSSION

Electrokinetic Properties of SiO_2 and Si_3N_4 Surfaces. The SiO_2- and Si_3N_4-coated Si wafers had ζ potentials of –98 ± 2 mV and –83 ± 1 mV, respectively, in 0.01 M NaCl buffered to pH 7.4 with 0.01 M HEPES (Figure 2). Both surfaces are strongly negatively charged with the Si_3N_4 surface being somewhat less negatively charged than the SiO_2 surface. This result is consistent with previously reported ζ values for Si_3N_4 and SiO_2 particles.[63,64]

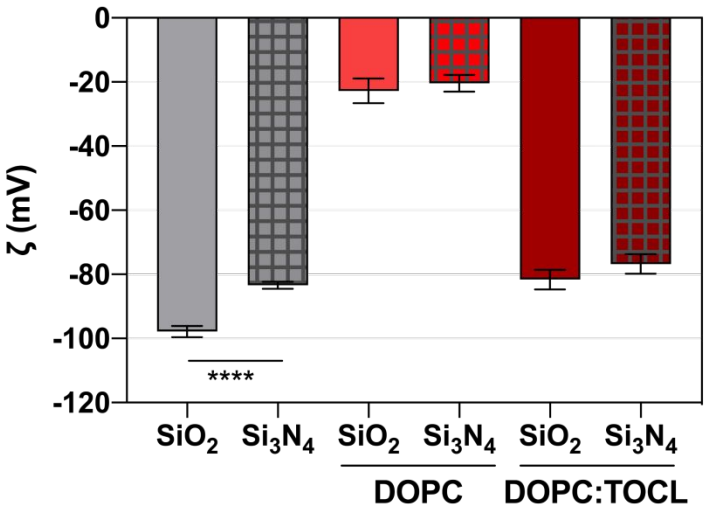

Figure 2. Zeta-potentials (ζ) of SiO_2- or Si_3N_4-coated Si wafers with and without supported lipid bilayers of the indicated composition calculated from streaming current measurements (Eq. 4). The DOPC:TOCL bilayers were composed of 91.2 mol% DOPC and 8.8 mol% TOCL. Measurements were conducted at 24-26 °C in 0.01 M NaCl buffered to pH 7.4 with 0.01 M HEPES. Bars are mean values; error bars represent one standard deviation of quadruplicate measurements.

We formed SLBs on the SiO_2- and Si_3N_4-coated wafers via the vesicle fusion method.[61] The ζ for the zwitterionic DOPC bilayer (–20 ±1 mV) was less negative than that of the underlying

SiO_2-coated wafer (Figure 2) and agrees well with the previously reported ζ for a DOPC bilayer on SiO_2 in 0.01 M KCl at pH 7.4 measured.[61] The ζ for bilayers formed from the 91.2% DOPC and 8.8 % dianionic TOCL were strongly negative (Figure 2); bilayers formed on the SiO_2-coated wafers had slightly more negative ζ than those on Si_3N_4 (–82 ± 3 mV vs. –77 ± 3 mV; $p = 0.0385$).

Influence of Sensor Coating on Formation of Supported Lipid Bilayers. Formation of bilayers with zwitterionic phospholipids on hydrophilic, negatively charged substrates consists of several steps: vesicle adsorption to a critical surface concentration (CSC), vesicle fusion and rupture accompanied by a release of solvent, and spontaneous assembly of the SLB.[48,55] We compared the impact of sensor coating on vesicle adsorption, rupture, bilayer formation, and stabilization using flat sensors that had been sputter coated with Si_3N_4 or SiO_2 (Figure S1a, Table 1). Attainment of the CSC is characterized by a minimum in the frequency response and a maximum in energy dissipation.

We compared the effect of sensor coating on the time to CSC (t_{CSC}) and the acoustic mass attained at the CSC ($\Gamma_{QCM\text{-}D,\ CSC}$). As the $\Delta D_7/(-\Delta f_7/7)$ values are all $< 0.2 \times 10^{-7}$ Hz^{-1} (Table S2), Kelvin-Voigt modeling was used to calculate the acoustic mass (Table 1). For the systems investigated, sensor coating has no discernible effect on t_{CSC} ($p < 0.05$) and a small effect on $\Gamma_{QCM\text{-}D,\ CSC}$ for only one bilayer composition ($p = 0.0235$; 60:20:20% DOPC:SM:Chol). The critical surface coverage was attained more rapidly for 91.2:8.8% DOPC:TOCL vesicles than for DOPC or 60:20:20% DOPC:SM:Chol vesicles due to the four-fold higher vesicle concentration used for the former (*vide supra*). As previously reported, the four-fold higher vesicle concentration facilitates formation of SLBs composed of 60:20:20% DOPC:SM:Chol.[6] These changes in frequency at CSC agree well with previous reports.[13,48]

Table 1. Time to reach the critical surface coverage (CSC) and surface mass densities at CSC and for the final bilayers formed on the indicated sensors.[a]

sensor properties			vesicle composition			CSC[b]		bilayer	
Topography	coating					t_{CSC}	Γ_{QCM-D}	Γ_{QCM-D}	Γ_{LSPR}
	material	method	DOPC	TOCL	SM/Chol	(s)	(ng·cm^{-2})	(ng·cm^{-2})	(ng·cm^{-2})
Flat	Si_3N_4	SC	100	–	–	469 ± 9	820 ± 64	420 ± 13	–
Flat	SiO_2	SC	100	–	–	440 ± 20	920 ± 22	439 ± 5	–
Flat	Si_3N_4	SC	91.2	8.8	–	110 ± 9	1010 ± 82	388 ± 5	–
Flat	SiO_2	SC	91.2	8.8	–	114 ± 7	900 ± 65	390 ± 8	–
Flat	Si_3N_4	SC	60	–	20/20	510 ± 61	1010 ± 31	460 ± 11	–
Flat	SiO_2	SC	60	–	20/20	460 ± 27	920 ± 19	481 ± 5	–
Reference	Si_3N_4	PECVD	91.2	8.8	–	110 ± 15	1200 ±160	390 ± 5	–
Protruding	Si_3N_4	PECVD	91.2	8.8	–	280 ± 12	987 ± 9	402 ± 27	359 ± 30
Flat	Si_3N_4	PECVD	91.2	8.8	–	230 ± 17	1020 ± 62	378 ± 10	333 ± 9

[a] Vesicle adsorption and rupture experiments were conducted in 0.15 M NaCl buffered to pH 7.4 with 0.010 M HEPES with 0.005 M $CaCl_2$ for 91.2:8.8 mol.% DOPC:TOCL vesicles and without $CaCl_2$ for DOPC and 60:20:20 mol.% DOPC:SM:Chol vesicles at 25 °C. The results are given by mean ± standard deviation of at least triplicate measurements. All values are for the 7th harmonic. Corresponding $\Delta f_7/7$ and ΔD_7 values are presented in Table S2. Abbreviations: Chol, cholesterol; CSC, critical surface coverage; DOPC, 1,2-dioleoyl-*sn*-glycero-3-phosphocholine; PECVD, plasma-enhanced chemical vapor deposition; SC, sputter coated; SM, sphingomyelin; TOCL, 1′,3′-bis[1,2-dioleoyl-*sn*-glycero-3-phospho]-*sn*-glycerol. [b] Time to reach the CSC and the total mass coupled to the sensor calculated *via* Kelvin-Voight modeling.

Phospholipid bilayers that had been rinsed with vesicle-free solution exhibited changes in frequency and dissipation (Table S2) generally consistent with prior reports.[13,48] For all bilayers, the value of $\Delta D_7/(\Delta f_7/7)$ was below 4×10^{-7} Hz^{-1} (Table S2) indicating that the bilayers formed can be regarded as laterally homogeneous rigid layers, permitting the Sauerbrey model[52] (Eq 1) to be employed to estimate the acoustic masses of the bilayers. For each bilayer composition, the final bilayer mass on the sensor, $\Gamma_{QCM-D,\,final}$, was statistically indistinguishable for the Si_3N_4- and SiO_2-coated sensors ($p > 0.05$; Table 1). The acoustic surface mass densities (Γ_{QCM-D}) of bilayers formed from 60:20:20% DOPC:SM:Chol on SiO_2 here (481 ± 5 ng·cm^{-2}) is the same as that in our previous work (482 ± 11 ng·cm^{-2}).[6] Further, the Γ_{QCM-D} of bilayers formed from 60:20:20% DOPC:SM:Chol vesicles were larger than those formed from DOPC or 91.2:8.8% DOPC:TOCL vesicles on the same substrate ($p \leq 0.015$). This is likely due to the higher lateral densities of lipids in the liquid ordered domains present in the 60:20:20% DOPC:SM:Chol bilayers but absent in the liquid disordered bilayers formed from of the other two compositions.[6]

Table 2. Initial attachment rates (r_d), acoustic surface mass densities (Γ_{QCM-D}), and optical surface mass densities (Γ_{LSPR}) for cytochrome *c* attachment to 91.2:8.8% DOPC:TOCL bilayers on the indicated sensors.[a]

sensor property				surface mass density (ng·cm^{-2})			
	Coating		r_d	maximum		after rinsing[c]	
topography	material	method[b]	(ng·cm^{-2}·s^{-1})	Γ_{QCM-D}	Γ_{LSPR}	Γ_{QCM-D}	Γ_{LSPR}
flat	Si_3N_4	SC	1.7 ± 0.1	270 ± 15	–	210 ± 10	–
flat	SiO_2	SC	2.2 ± 0.4	280 ± 7	–	210 ± 12	–
reference[d]	Si_3N_4	PECVD	1.9 ± 0.2	270 ± 12	–	180 ± 19	–
protruding	Si_3N_4	PECVD	0.7 ± 0.1	270 ± 6	57 ± 3	191 ± 8	23 ± 1
flat	Si_3N_4	PECVD	0.8 ± 0.1	254 ± 7	50 ± 6	184 ± 9	16 ± 4

[a] Experiments were conducted in 0.010 M NaCl buffered to pH 7.4 with 0.010 M HEPES at 25 °C. For the acoustic surface mass densities, the corresponding frequency and dissipation data are given in Table S3. Values are means ± standard deviations of at least triplicate experiments. Abbreviations: DOPC, 1,2-dioleoyl-*sn*-glycero-3-phosphocholine; PECVD, plasma-enhanced chemical vapor deposition; SC, sputter coating; TOCL, 1′,3′-bis[1,2-dioleoyl-*sn*-glycero-3-phospho]-*sn*-glycerol.
[b] Data for the frequency and dissipation shifts for cytochrome *c* are after attachment of 30 min and then stabilization for 30 min prior to rinsing with cytochrome *c*-free solution.
[c] After rinsing 20 min with cytochrome *c*-free solution.
[d] Measurements conducted using window cell.

Influence of Sensor Coating on Cytochrome *c* Attachment to Supported Lipid Bilayers. We first used cytochrome *c*, a peripheral membrane protein with an approximate +8 charge at pH 7.4, to test the influence of sensor coating on attachment to supported lipid bilayers. Cytochrome *c* interacts with the distal leaflet TOCL-containing bilayers primarily via electrostatic attraction.[9] Introduction of cytochrome *c* into the flow cell containing a pre-formed 91.2:8.8% DOPC:TOCL bilayer resulted in an abrupt decrease in frequency, followed by a much slower decline (Figure S1b) indicating high affinity of the protein molecules for the bilayers formed on the sensors. The frequency traces for cytochrome *c* adsorption almost overlapped for Si_3N_4- and SiO_2-coated sensors. Initial rates of cytochrome *c* attachment to the supported 91.2:8.8% DOPC:TOCL bilayers did not differ for the Si_3N_4- and SiO_2-coated sensors (Table 2). After maximum acoustic surface mass densities had been attained as well as after 20 min rinsing with cytochrome *c*-free solution, $\Delta D_7/(-\Delta f_7/7)$ values were below 4×10^{-7} Hz^{-1} allowing the Sauerbrey relationship to be applied.[50] The surface mass densities of cytochrome *c* did not differ for the

DOPC:TOCL bilayers supported by Si_3N_4- or SiO_2-coated sensors for either the maximum value or that obtained after 20-min rinsing with 0.01 NaCl ($p > 0.05$; Table 2). The rinse removed ~24% of proteins from the bilayer surfaces. These data demonstrate that the rate and extent of cytochrome *c* attachment to DOPC:TOCL bilayers is insensitive to the choice of Si_3N_4 or SiO_2 for supporting the bilayer. The DOPC:TOCL bilayers exhibit statistically indistinguishable ζ. The large difference in Hamaker constant between the two bulk substates does not appear to impact cytochrome *c* attachment to the bilayers.

Influence of Sensor Coating on PDDA-QD Attachment to Supported Lipid Bilayers. As a second test of the influence of the underlying substrate on interactions with supported lipid bilayers, we examined the initial rates of PDDA-QD attachment to bilayers composed of DOPC or 60:20:20% DOPC:SM:Chol supported by Si_3N_4 or SiO_2 substrates, as well as changes in frequency and dissipation at maximal coverage and after rinsing (Table 3). (Because $D_7/(\Delta f_7/7)$ values for some measurements were near 4×10^{-7} Hz^{-1}, we report the frequency and dissipation values rather than estimate acoustic surface mass densities.) For DOPC bilayer, the initial rate of attachment and frequency changes at maximal surface coverage and after rinsing were higher for the bilayer formed on SiO_2 than on Si_3N_4 ($p \leq 0.0479$). These results appear to reflect a higher affinity for and retention of positively charged PDDA-QDs by DOPC bilayers supported on the more negatively charged SiO_2 vs. the Si_3N_4 coating. The ζ values for DOPC bilayers on the two substrates were statistically indistinguishable (Figure 3). This implies that interactions other than simple electrostatic attraction between the nanoparticle and the bilayer were responsible for the preferential interaction of PDDA-QDs with the bilayer on the SiO_2 substrate. Furthermore, the Hamaker constant for SiO_2 is smaller than that for Si_3N_4 (*vide supra*) suggesting weaker van der Waals interactions with the PDDA-QDs. We hypothesize that the preferential

attachment of PDDA-QDs to and their retention by the DOPC bilayer on SiO_2 relative to that on Si_3N_4 was due to the penetration of the PDDA coating into the bilayer and interaction with the substrate. PDDA-QDs have been shown to induce structural rearrangement to DOPC bilayers, apparently due to the penetration of the PDDA coating into the bilayer.[46] Penetration of the PDDA into the bilayer causes an increase in the energy dissipation by the nanoparticle-bilayer system. The dissipation shift measured is nearly identical to that as previously reported.[46] This process may be more sensitive to the charge of the underlying substrate than is the non-penetrative association of cytochrome *c* with the distal leaflet of the bilayer.[9]

Bilayers composed of 60/20/20% DOPC/SM/Chol form phase-segregated domains (liquid-ordered domains enriched in SM and Chol within a liquid-disordered phase enriched in DOPC) on SiO_2 substrates.[6] Initial rates of PDDA-QD attachment to these bilayers was insensitive to whether SiO_2 or Si_3N_4 was the substrate, as was the frequency change after rinsing ($p > 0.05$). Interaction of PDDA-QDs with these bilayers exhibits the same structural rearrangements of the liquid-disordered phase as seen in DOPC, but also the destabilization of the liquid-ordered domains, possibly due to the additional energy of polymer-coated nanoparticle collisions at the bilayer surface exceeding the free energy of membrane mixing between the liquid-ordered and -disordered phases.[46] The data in hand do not permit drawing a strong conclusion regarding these bilayers. Domain structure may differ on the two substrates in a manner that influences the rate and extent of PDDA-QD attachment.

Influence of Si_3N_4 Coating Method on Supported Lipid Bilayer Formation and Subsequent Interaction with Cytochrome *c*. Sputter coating and plasma enhanced chemical vapor deposition have been used to coat commercial QCM-D sensors with Si_3N_4. We investigated whether these coating methods resulted in discernable differences to the formation of supported

91.2:8.8% DOPC:TOCL bilayers and the subsequent attachment of cytochrome *c*. For these experiments we used a Si_3N_4-coated QCM-D sensor from Biolin and one from Insplorion that lacked nanoplasmonic disks (denoted "reference" in Tables 1 and 2). No differences were observed in t_{csc}, $\Gamma_{QCM\text{-}D}$ at the CSC, or $\Gamma_{QCM\text{-}D}$ for the bilayer ($p > 0.05$; Table 1) indicating that the coating method had no detectable effect on the interactions of the vesicles with the Si_3N_4 surfaces or the formation of the bilayer. Given the similarity of the bilayers formed on the two Si_3N_4 coatings, the equivalence of the initial rate of attachment for and surface mass densities achieved by cytochrome *c* was not surprising ($p > 0.05$; Table 2). The coating method had no effect on the attachment of the protein molecules to the SLBs formed on the sensors.

Table 3. Initial attachment rates (r_d) and changes in frequency (Δf) and dissipation (ΔD) upon interaction of PDDA-QDs with supported lipid bilayers of the indicated composition.[a]

					attachment			
	vesicle composition (mol%)				maximum[b]		after rinse[c]	
Sensor Coating	DOPC	SM	Chol	r_d (ng·cm^{-2}·s^{-1})	$\Delta f_7/7$ (Hz)	ΔD_7 (10^{-6})	$\Delta f_7/7$ (Hz)	ΔD_7 (10^{-6})
Si_3N_4	100	–	–	1.4 ± 0.4	–18 ± 1.1	1.7 ± 0.1	–10 ± 1.6	2.8 ± 0.3
SiO_2	100	–	–	2.4 ± 0.4	–20 ± 1.2	1.8 ± 0.1	–16 ± 2.2	3.3 ± 0.4
Si_3N_4	60	20	20	2.0 ± 0.5	–18.7 ± 0.9	1.6 ± 0.1	–13.1 ± 0.4	3.6 ± 0.2
SiO_2	60	20	20	1.4 ± 0.6	–16.4 ± 0.7	1.3 ± 0.1	–13 ± 2.6	3.0 ± 0.4

[a] Experiments were conducted in 0.010 M NaCl buffered to pH 7.4 with 0.010 M HEPES at 25 °C. All data are the 7th harmonic. Values are means ± standard deviations of at least triplicate experiments. Abbreviations: DOPC, 1,2-dioleoyl-*sn*-glycero-3-phosphocholine; SM, sphingomyelin; Chol, cholesterol. [b] Data for the frequency and dissipation shifts for PDDA-QD after 20 min attachment. [c] After 20 min rinse with 0.01 M NaCl.

Optical Properties of Nanoplasmonic Sensors Differing in Topography. Sensors for simultaneous QCM-D measurement and nanoplasmonic sensing can be fabricated with a variety of topographies. Here we compare the optical properties of sensors with nanoplasmonic gold disks assembled atop vs. embedded in the SiO_2 substrate prior to overcoating with Si_3N_4. The resulting sensors had respectively a surface characterized by nanoplasmonic disks protruding above the plane of the (Si_3N_4-coated) sensor or a flat surface. The two topographies result in differences in the average dielectric constant of the medium in direct contact with the gold.

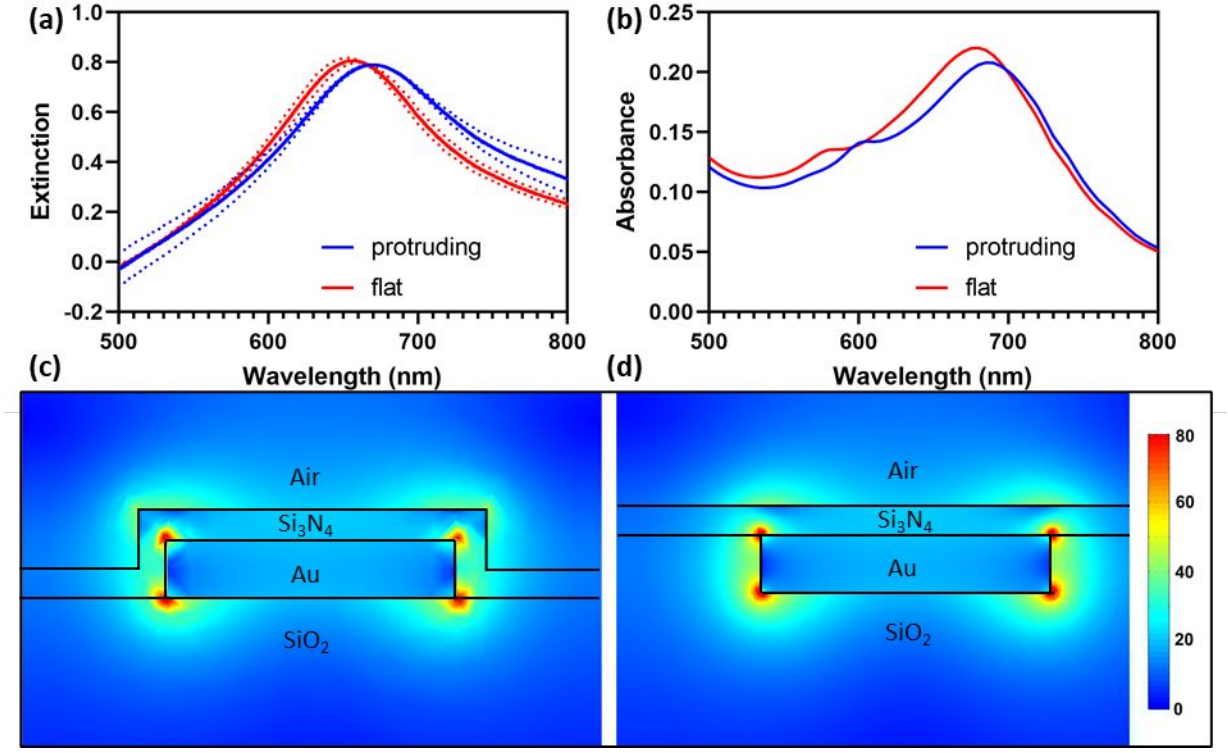

Figure 3. (a) Experimental and (b) simulated extinction spectra for the NPS sensors in air. Experimental spectra are the means of three replicate sensors. Dotted lines indicate one standard deviation (c) Protruding and (d) flat simulated scattered field amplitude distributions around the nanoplasmonic disks. Colorbar is a unitless electromagnetic field enhancement factor taken from the simulation.

We characterized the localized surface plasmon resonance response of these sensors prior to forming supported phospholipid bilayers on them. Figure 3a shows the extinction peaks of the NPS sensors recorded in air. Excitation peak wavelength and extinction are provided in Table S5. The maximum extinction peak (λ_{max}) for the flat sensor exhibited a hypsochromic shift (blue shift) relative to that for the sensor with protruding nanoplasmonic disks. The reason for the difference in λ_{max} is that for the flat sensor the nanoplasmonic gold disks have a smaller fraction of their surface in direct contact with Si_3N_4 with its higher index of refraction of $n_{Si_3N_4}$ ~2.00, compared with n_{SiO_2} ~1.47 (Figure 1) resulting in a higher effective refractive index for the protruding

geometry. Our results are consonant with those previously reported for SiO_2-coated sensors.[45] where the λ_{max} for an SiO_2-coated flat sensor was found both experimentally and theoretically to be blue shifted relative to a SiO_2-coated protruding sensor. Because the evanescent electromagnetic field decays more slowly in a high-index material, the Si_3N_4-coated protruding sensors also yield a larger effective sensing volume the adjacent medium, such as air or water. Finite-difference time-domain simulations demonstrated that the sensing volume for a protruding disk was larger than that of the embedded disk by ~70% and that the energy density was ~2.8 times larger.[45] Figure 3b shows the results of our electromagnetic field simulations for the flat and protruding geometries in air. The protruding and flat geometries yields similar resonance curves, with that of the protruding sensor shifted 5 nm longer in wavelength compared with the flat sensor, in qualitative agreement with the experiments and with prior studies using SiO_2-coated sensors.

A prior comparison of flat vs. protruding sensors found that the sensitivity of flat sensors was lower than that of sensors with protruding nanoplasmonic disks.[45] We used graded concentrations of glycerol (0-35 wt % in 5 wt % steps)[4] to determine the bulk refractive index sensitivity of the sensors (Figure S2). The bulk refractive index sensitivity for bare sensors with protruding and embedded nanoplasmonic disks (S) were 109 ± 1.0 nm RIU^{-1} and 89 ± 1.0 nm RIU^{-1}, respectively. As expected, the sensors with protruding nanoplasmonic disks were more sensitive to changes in bulk refractive index. After formation of a 91.2:8.8% DOPC:TOCL bilayer, a fraction of the total LSPR field intensity was occupied by the SLB, and thus the bulk refractive index sensitivity was reduced for both sensors. The bulk refractive index sensitivity after bilayer formation (S') for the sensors with protruding and embedded nanoplasmonic disks were 90.4 ± 0.5 nm RIU^{-1} and 73.0 ± 0.4 nm RIU^{-1}, respectively. The presence of a supported phospholipid bilayer

attenuated the bulk refractive index sensitivity by 17-18% for sensors with protruding and embedded nanoplasmonic disk.

Effect of Sensor Topography on Supported Lipid Bilayer Formation. We next examined the extent to which sensor topography impacted the formation of supported 91.2:8.8% DOPC:TOCL bilayers on Si_3N_4-coated sensors. Use of QCM-D sensors with nanoplasmonic disks allows simultaneous measurement of acoustic and optical mass. Representative data obtained from the combination of NPS and QCM-D are presented in Figure S3. The QCM-D frequency and dissipation responses exhibited the same features characteristic for the formation of a supported lipid bilayer by the vesicle fusion method (*vide supra*; Figure S1a). The kinetics of supported phospholipid bilayer formation were more rapid for the sensor with embedded than with protruding nanoplasmonic disks: the time to attain CSC was shorter for the flat sensor ($p = 0.0176$; Table 1) as was the time to formation of a stable bilayer (not shown). Sensor topography did not influence the acoustic surface mass densities of the vesicles at the CSC or of the stable bilayers ($p > 0.05$; Table 1).

The LSPR response was characterized by a monotonic increase in λ_{max} until a plateau is attained (Figure 4a). After bilayer formation, the sensor with protruding nanoplasmonic disks had a larger $\Delta\lambda_{max}$ than did the flat sensor due to the larger sensing volume and thus higher overall sensitivity.[45] Close inspection of the LSPR signal trace reveals the presence of an inflection point at which the rate of change in λ_{max} accelerates. This inflection point coincides with the time point at which changes in QCM-D frequency and dissipation signal the commencement of vesicle fusion and rupture initiating the assembly of a supported lipid bilayer as has been previously described.[4,13,34] To compare the LSPR responses for the sensors with protruding and embedded nanoplasmonic disks, we followed the approach of Nugroho et al.[45] To facilitate qualitative

comparison, we normalized the LSPR traces to the maximum $\Delta\lambda_{max}$ attained for each sensor and indicated the two regimes that are dominated by different processes: (I) adsorption of phospholipid vesicles to the sensor surface and (II) vesicle rupture and spreading of the supported lipid bilayer (Figure 4b). The kinetics of vesicle adsorption (regime I) were nearly identical for the two sensor topographies. In contrast, the rate of change in λ_{max} after the inflection point (regime II) was steeper for the flat sensor than for the sensor with protrusions indicating that the kinetics of vesicle rupture and bilayer spreading was more rapid for the former topography. To quantitatively analyze our kinetics data, we plotted the first derivative of the normalized $\Delta\lambda_{max}$ with respect to time as a function of time (Figure 4c). As expected, regimes I and II were clearly separated. The rates of vesicle adsorption (regime I) to the sensor surface were identical for the two topographies, reaching a maximum normalized $\Delta\lambda_{max}$ of 0.19 (± 0.01) min^{-1}. The rate of vesicle rupture was substantially larger on flat sensor (maximum normalized $\Delta\lambda_{max}$ = 0.37 (± 0.01) min^{-1}) than on that with protrusions (maximum normalized $\Delta\lambda_{max}$ = 0.26 (± 0.01) min^{-1}; one-tailed *t*-test, $p = 0.0308$). The maximum vesicle rupture rate on the sensor with protrusions was 78 ± 3% ($n = 3$) that on flat sensor. The slower rate of bilayer spreading on the sensor with protrusions relative to the flat sensor is attributable to the free energy penalty associated with the bending of the bilayer required for it to conform to the substrate topography.[65,66] These findings are congruent with those reported previously for POPC vesicles and flat and corrugated SiO_2-coated nanoplasmonic sensors.[45]

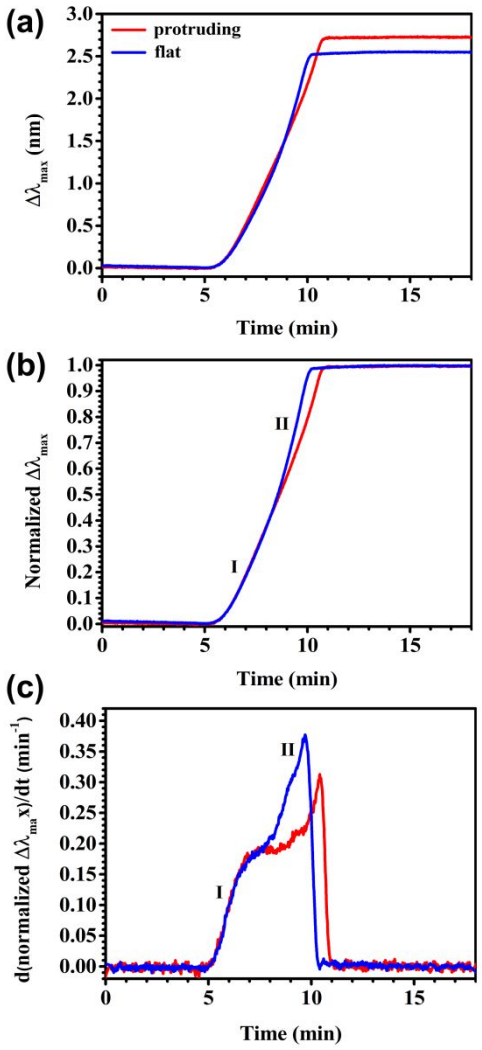

Figure 4. Optical sensing of supported lipid bilayer formation on sensors differing in topography: (a) original and (b) normalized temporal evolution of the shift in the extinction peak maximum ($\Delta\lambda_{max}$) for flat sensors and those with protrusions upon exposure to 91.2:8.8 mol% DOPC:TOCL vesicles, (c) vesicle adsorption and rupture rates on the two sensors, represented by the first derivatives of the normalized $\Delta\lambda_{max}$. Representative data of triplicate experiments.

Sensor topography did not impact the optical surface mass density of the bilayers (Table 1). The difference between the acoustic and optical surface mass densities of the bilayers reflects the amount of solvent hydrodynamically coupled to the oscillations of the sensor. Solvent mass associated with the supported 91.2:8.8% DOPC:TOCL bilayers was 12 ± 4%. If we attribute all of the dynamically coupled solvent to the solvent layer between the bilayer and the sensor surface

and assume that the density of this interfacial solvent is the same as bulk water, the thicknesses of this solvent layer are 0.43 (± 0.16) nm and 0.45 (± 0.01) nm for the sensors with protruding and embedded nanoplasmonic disks, respectively. This analysis likely overestimates the thickness of the solvent layer between the sensor surface and the bilayer due to the higher density of interfacial water.[67] Subtracting the water layer thickness from the total Sauerbrey thickness, the thicknesses of the SLBs on the two sensors were statistically indistinguishable (i.e., 3.6 ± 0.3 nm and 3.3 ± 0.1 nm for protruding and flat sensors, respectively). X-ray scattering studies have determined the average thicknesses of simple phospholipid/cholesterol bilayers of the endoplasmic reticulum, Golgi apparatus, and basolateral and apical plasma membranes of rat hepatocytes to be 3.75 ± 0.04 nm, 3.95 ± 0.04 nm, 3.56 ± 0.06 nm, and 4.25 ± 0.03 nm, respectively.[68]

Influence of Sensor Topography on Cytochrome *c* Adsorption to Supported Phospholipid Bilayers. We next investigated the extent to which the topography of bilayer-coated sensors with embedded or protruding nanoplasmonic disks impacted protein adsorption and desorption. For these experiments we employed bilayers composed of 91.2:8.8 mol% DOPC:TOCL and the peripheral membrane protein cytochrome *c*. The LSPR traces for cytochrome *c* adsorption had nearly the same initial shapes for the two sensors (Figure 5a). Adsorption occurred rapidly and approached a plateau within ~10 min. Normalization of the LSPR traces demonstrates that the initial rate of increase in $\Delta\lambda_{max}$ was identical for the flat sensors and those with protrusions (Figure 5b, Table 2); initial adsorption rates of cytochrome *c* to bilayers on the flat sensors and those with protrusions were statistically indistinguishable (0.8 (± 0.1) and 0.7 (± 0.1) $ng \cdot cm^{-2} \cdot s^{-1}$, respectively. The independence of initial cytochrome *c* adsorption to the bilayer from sensor topography reflects the strong electrostatic attraction of the positively charged protein to the negatively charged TOCL lipids in the bilayer. As the surface of the bilayer approached

saturation with cytochrome *c*, the rate of adsorption slowed. This was more pronounced for the bilayer formed on the flat sensors than that on the sensor with protrusions. This may be related to the negative curvature of the conformal bilayer formed on the sensor with protrusions which may have favored the accumulation of TOCL.[9,69]

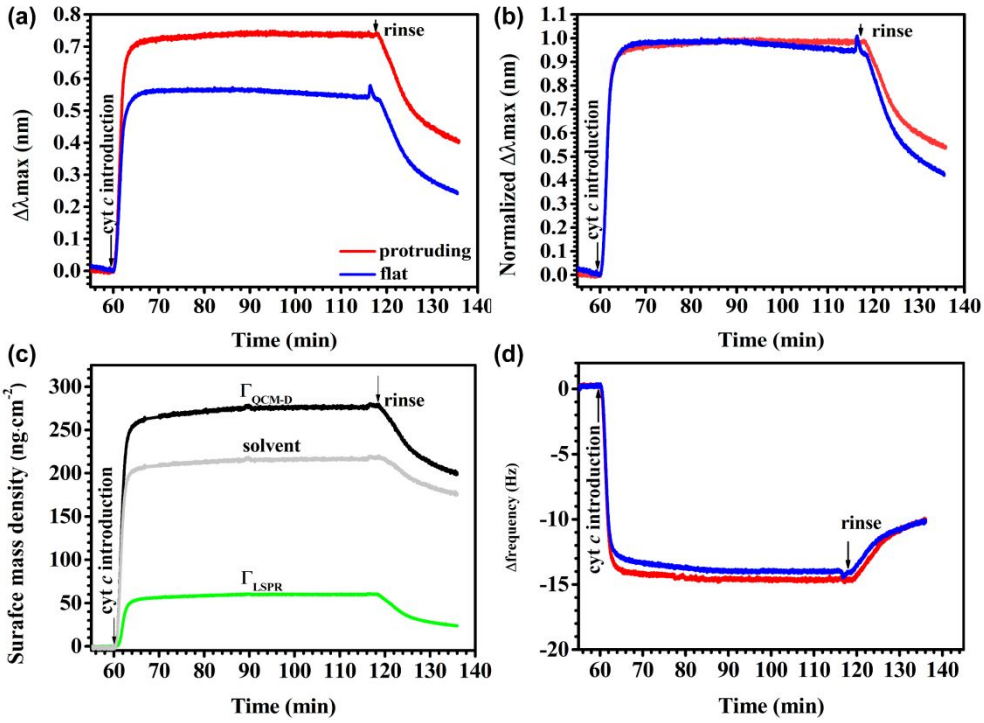

Figure 5. Adsorption and desorption of cytochrome *c* to 91.2:8.8 mol% DOPC:TOCL bilayers formed on flat sensors and those with protrusions: (a) original and (b) normalized temporal evolution of $\Delta\lambda_{max}$, (c) a typical comparison of acoustic ($\Gamma_{QCM\text{-}D}$), optical (Γ_{LSPR}) and solvent surface mass densities, (d) corresponding QCM-D changes in frequency for the 7th harmonic.

We calculated the optical (Γ_{LSPR}) and acoustic ($\Gamma_{QCM\text{-}D}$) surface mass densities of cytochrome *c* on the bilayers formed on the two sensors using the de Feijter equation[4,70–72] and the Sauerbrey model[52] (assuming a laterally homogeneous cytochrome *c* adlayer), respectively, as previously described.[9] The solvent mass is the difference between the acoustic and optical masses. The optical surface mass density of stabilized protein layers on bilayers formed on flat sensors was slightly lower than those on sensors with protrusions before rinsing (50 ± 6 ng·cm^{-2} and 57 ± 3 ng·cm^{-2},

respectively; one-tailed *t*-test, $p = 0.0453$). Similarly, the acoustic surface mass density of cytochrome *c* was slightly lower for bilayer formed on the flat sensor than on the sensor with protrusions (254 ± 7 ng·cm^{-2} and 270 ± 6 ng·cm^{-2}, respectively; one-tailed *t*-test, $p = 0.0155$). The maximum $\Gamma_{QCM\text{-}D}$ of cytochrome *c* exceeded that of the Γ_{LSPR} by a factor of ~5 due to the hydrodynamically coupled solvent sensed by QCM-D (Figure 5c).

After rinsing the cytochrome *c* adlayer for 20 min with a protein-free solution, the protein acoustic surface mass density was indistinguishable on the bilayers formed on the two sensors, as was the optical mass density ($p > 0.05$ for both). Rinsing removed the same proportion of cytochrome *c* or dynamically coupled solvent water from the bilayers formed on the flat sensor and the sensor with protrusions ($p > 0.05$). However, the initial desorption rates of cytochrome *c* from the bilayers formed on protruding sensors were 8 ± 1 % larger than those on flat sensors. This may suggest that the flat sensor can bind proteins slightly more strongly than sensors with protrusions.

CONCLUSIONS

Silica-coated sensors exhibited more negative zeta-potentials than those coated with Si_3N_4. Despite this, the coating had almost no effect on the rates of phospholipid vesicle adsorption or rupture during the formation of single-component DOPC or multi-component DOPC+TOCL and DOPC+SM+Chol supported lipid bilayers. The coatings also had nearly no effect on subsequent adsorption of cytochrome *c* to the SLBs. In contrast, the interactions of polycation (PDDA)-wrapped QDs with single component DOPC SLBs depended on the substrate: PDDA-QDs had a higher affinity for SiO_2- over Si_3N_4-coatings. Increased adsorption of PDDA QDs on SiO_2-coated sensors is attributed to the increased electrostatic attraction between the positively charged QDs and the negatively charged SLB. Adsorption of PDDA-QD to 60:20:20% DOPC:SM:Chol bilayers

was insensitive to whether SiO_2- or Si_3N_4-coated sensors were used, as was the degree of adsorption reversibility.

The wavelength of maximum extinction for the sensor with protruding nanoplasmonic disks exhibited a hypsochromic shift, higher bulk refractive index sensitivity, and a larger sensing volume relative to the topographically flat sensor with embedded nanoplasmonic disks. The vesicle adsorption rates on protruding and flat sensors were nearly identical, but the vesicle rupture rate on the protruding sensor was only 78 ± 3% that on the flat sensor. The acoustic and optical surface mass densities of the supported lipid bilayer on the protruding and flat sensors were statistically indistinguishable; however, the acoustic and optical masses of the adsorbed protein layers on the protruding sensors were slightly higher than that on flat sensors before rinse. Although the presence of gold nanodisks under the Si_3N_4 coating decreased the initial adsorption rate of cytochrome *c*, adsorption kinetics on the two sensors with different topographies were nearly the same, and the desorption of the proteins from the SLBs on the protruding sensors was slightly higher than that on the flat sensor.

Contrary to a prior report of increased sensitivity for protruding sensors relative to flat sensors,[45] our results suggest that the sensitivities are not distinguishable. The plasmonic resonance frequency is controlled primarily by the average dielectric constant of the region within the evanescent plasmonic electromagnetic wave. While sensors with a protruding geometry have a larger net area in contact with the adjacent liquid medium, the net change in average dielectric constant resulting for protein adsorption is expected to be similar for both geometries. The findings presented here can guide the choice of sensors composition and topography in studying the interactions of protein or nanoparticles with supported lipid bilayers by the combination of QCM-D and NPS.

AUTHOR INFORMATION

Corresponding Author

Joel A. Pedersen – *Departments of Soil Science, Civil & Environmental Engineering, and Chemistry, University of Wisconsin, Madison, WI 53076, United States*; orcid.org/0000-0002-3918-1860; e-mail joelpedersen@wisc.edu.

Authors

Hui Yin – *Key Laboratory of Arable Land Conservation (Middle and Lower Reaches of Yangtse River), Ministry of Agriculture and Rural affairs, College of Resources and Environment, Huazhong Agricultural University, Wuhan 430070, P.R. China*; orcid.org/0000-0003-3060-7025

Arielle Mensch – *Department of Chemistry, University of Wisconsin, Madison, WI 53706, United States*; orcid.org/0000-0002-4063-5882

Christian A. Lochbaum – *Department of Chemistry, University of Wisconsin, Madison, WI 53706, United States*; orcid.org/0000-0002-1955-2118

Isabel U. Foreman-Ortiz – *Department of Chemistry, University of Wisconsin, Madison, WI 53706, United States*; orcid.org/0000-0003-3169-7026

Emily R. Caudill – *Department of Chemistry, University of Wisconsin, Madison, WI 53706, United States*; orcid.org/0000-0002-3645-9804

Present address: *Feather River College, Quincy, CA 95971, United States*

Robert J. Hamers – *Department of Chemistry, University of Wisconsin, Madison, WI 53706, United States*; orcid.org/0000-0003-3821-9625

Notes

The authors declare no competing financial interest.

ACKNOWLEGEMENTS

This work was supported by the National Science Foundation under the Center for Sustainable Nanotechnology (CHE-2001611). HY gratefully acknowledges funding from China Scholarship Council. JAP gratefully acknowledges support from the William A. Rothermel Bascom Professorship and a Vilas Distinguished Achievement Professorship. We thank Saima Zaman (Insplorion) for acquiring the NPS spectra in air, ~~and~~ Jennifer Andersson (Insplorion) for helpful discussions, and Rigoberto Hernandez, Qiang Cui, and Emily Tollefson for their contributions to the TOC artwork.

ABBREVIATIONS

Chol, cholesterol; CSC, critical surface coverage; d_h, hydrodynamic diameter; DOPC, 1,2-dioleoyl-*sn*-glycero-3-phosphocholine; HEPES, 2-[4-(2-hydroxyethyl)piperazin-1-yl] ethanesulfonic acid; LSPR, localized surface plasma resonance; NP, nanoparticles; NPS, nanoplasmonic sensing; PDDA-QD, poly(diallyldimethylammonium chloride) polymer wrapped CdSe/ZnS core/shell quantum dot; PECVD, plasma-enhanced chemical vapor deposition; POPC, palmitoyl-2-oleoyl-*sn*-glycero-3-phosphocholine; QCM-D, quartz crystal microbalance with dissipation monitoring; SLB, supported lipid bilayers; SM, sphingomyelin; TOCL, 1′,3′-bis[1,2-dioleoyl-*sn*-glycero-3-phospho]-*sn*-glycerol; Γ_{LSPR}, optical surface mass density; Γ_{QCM-D}, acoustic surface mass density; ζ, zeta potential.

REFERENCES

(1) Wargenau, A.; Schulz, S.; Hakimzadeh, A.; Tufenkji, N. Evaluating the Cell Membrane Penetration Potential of Lipid-Soluble Compounds Using Supported Phospholipid Bilayers. *Anal. Chem.* **2018**, *90* (19), 11174–11178. https://doi.org/10.1021/acs.analchem.8b02207.

(2) Fitzgerald, N. J. M.; Wargenau, A.; Sorenson, C.; Pedersen, J.; Tufenkji, N.; Novak, P. J.; Simcik, M. F. Partitioning and Accumulation of Perfluoroalkyl Substances in Model Lipid Bilayers and Bacteria. *Environ. Sci. Technol.* **2018**, *52* (18), 10433–10440. https://doi.org/10.1021/acs.est.8b02912.

(3) Wang, K. F.; Nagarajan, R.; Camesano, T. A. Differentiating Antimicrobial Peptides Interacting with Lipid Bilayer: Molecular Signatures Derived from Quartz Crystal Microbalance with Dissipation Monitoring. *Biophys. Chem.* **2015**, *196*, 53–67. https://doi.org/https://doi.org/10.1016/j.bpc.2014.09.003.

(4) Jonsson, M. P.; Jönsson, P.; Höök, F. Simultaneous Nanoplasmonic and Quartz Crystal Microbalance Sensing: Analysis of Biomolecular Conformational Changes and Quantification of the Bound Molecular Mass. *Anal. Chem.* **2008**, *80* (21), 7988–7995. https://doi.org/10.1021/ac8008753.

(5) Glasmästar, K.; Larsson, C.; Höök, F.; Kasemo, B. Protein Adsorption on Supported Phospholipid Bilayers. *J. Colloid Interface Sci.* **2002**, *246* (1), 40–47. https://doi.org/https://doi.org/10.1006/jcis.2001.8060.

(6) Melby, E. S.; Mensch, A. C.; Lohse, S. E.; Hu, D.; Orr, G.; Murphy, C. J.; Hamers, R. J.; Pedersen, J. A. Formation of Supported Lipid Bilayers Containing Phase-Segregated Domains and Their Interaction with Gold Nanoparticles. *Environ. Sci. Nano* **2016**, *3* (1), 45–55. https://doi.org/10.1039/C5EN00098J.

(7) Min, H.; Freeman, E.; Zhang, W.; Ashraf, C.; Allara, D.; van Duin, A. C. T.; Tadigadapa, S. Modified Random Sequential Adsorption Model for Understanding Kinetics of Proteins Adsorption at a Liquid–Solid Interface. *Langmuir* **2017**, *33* (29), 7215–7224. https://doi.org/10.1021/acs.langmuir.7b00523.

(8) Mensch, A. C.; Hernandez, R. T.; Kuether, J. E.; Torelli, M. D.; Feng, Z. V.; Hamers, R. J.; Pedersen, J. A. Natural Organic Matter Concentration Impacts the Interaction of Functionalized Diamond Nanoparticles with Model and Actual Bacterial Membranes. *Environ. Sci. Technol.* **2017**, *51* (19), 11075–11084. https://doi.org/10.1021/acs.est.7b02823.

(9) Melby, E. S.; Allen, C.; Foreman-Ortiz, I. U.; Caudill, E. R.; Kuech, T. R.; Vartanian, A. M.; Zhang, X.; Murphy, C. J.; Hernandez, R.; Pedersen, J. A. Peripheral Membrane Proteins Facilitate Nanoparticle Binding at Lipid Bilayer Interfaces. *Langmuir* **2018**, *34* (36), 10793–10805. https://doi.org/10.1021/acs.langmuir.8b02060.

(10) Yousefi, N.; Tufenkji, N. Probing the Interaction between Nanoparticles and Lipid Membranes by Quartz Crystal Microbalance with Dissipation Monitoring . *Frontiers in Chemistry* . 2016, p 46.

(11) Richter, R. P.; Bérat, R.; Brisson, A. R. Formation of Solid-Supported Lipid Bilayers: An Integrated View. *Langmuir* **2006**, *22* (8), 3497–3505. https://doi.org/10.1021/la052687c.

(12) Richter, R. P.; Brisson, A. R. Following the Formation of Supported Lipid Bilayers on Mica: A Study Combining AFM, QCM-D, and Ellipsometry. *Biophys. J.* **2005**, *88* (5), 3422–3433. https://doi.org/https://doi.org/10.1529/biophysj.104.053728.

(13) Ferhan, A. R.; Jackman, J. A.; Cho, N.-J. Probing Spatial Proximity of Supported Lipid

Bilayers to Silica Surfaces by Localized Surface Plasmon Resonance Sensing. *Anal. Chem.* **2017**, *89* (7), 4301–4308. https://doi.org/10.1021/acs.analchem.7b00370.

(14) Howland, M. C.; Szmodis, A. W.; Sanii, B.; Parikh, A. N. Characterization of Physical Properties of Supported Phospholipid Membranes Using Imaging Ellipsometry at Optical Wavelengths. *Biophys. J.* **2007**, *92* (4), 1306–1317. https://doi.org/https://doi.org/10.1529/biophysj.106.097071.

(15) Merz, C.; Knoll, W.; Textor, M.; Reimhult, E. Formation of Supported Bacterial Lipid Membrane Mimics. *Biointerphases* **2008**, *3* (2), FA41–FA50. https://doi.org/10.1116/1.2896119.

(16) Sugihara, K.; Delai, M.; Szendro, I.; Guillaume-Gentil, O.; Vörös, J.; Zambelli, T. Simultaneous OWLS and EIS Monitoring of Supported Lipid Bilayers with the Pore Forming Peptide Melittin. *Sensors Actuators B Chem.* **2012**, *161* (1), 600–606. https://doi.org/https://doi.org/10.1016/j.snb.2011.11.007.

(17) Parkkila, P.; Elderdfi, M.; Bunker, A.; Viitala, T. Biophysical Characterization of Supported Lipid Bilayers Using Parallel Dual-Wavelength Surface Plasmon Resonance and Quartz Crystal Microbalance Measurements. *Langmuir* **2018**, *34* (27), 8081–8091. https://doi.org/10.1021/acs.langmuir.8b01259.

(18) Mashaghi, A.; Swann, M.; Popplewell, J.; Textor, M.; Reimhult, E. Optical Anisotropy of Supported Lipid Structures Probed by Waveguide Spectroscopy and Its Application to Study of Supported Lipid Bilayer Formation Kinetics. *Anal. Chem.* **2008**, *80* (10), 3666–3676. https://doi.org/10.1021/ac800027s.

(19) Daly, C. A.; Allen, C.; Rozanov, N.; Chong, G.; Melby, E. S.; Kuech, T. R.; Lohse, S. E.; Murphy, C. J.; Pedersen, J. A.; Hernandez, R. Surface Coating Structure and Its Interaction with Cytochrome c in EG6-Coated Nanoparticles Varies with Surface Curvature. *Langmuir* **2020**, *36* (18), 5030–5039. https://doi.org/10.1021/acs.langmuir.0c00681.

(20) Reimhult, E.; Höök, F.; Kasemo, B. Intact Vesicle Adsorption and Supported Biomembrane Formation from Vesicles in Solution: Influence of Surface Chemistry, Vesicle Size, Temperature, and Osmotic Pressure. *Langmuir* **2003**, *19* (5), 1681–1691. https://doi.org/10.1021/la0263920.

(21) Ferhan, A. R.; Špačková, B.; Jackman, J. A.; Ma, G. J.; Sut, T. N.; Homola, J.; Cho, N.-J. Nanoplasmonic Ruler for Measuring Separation Distance between Supported Lipid Bilayers and Oxide Surfaces. *Anal. Chem.* **2018**, *90* (21), 12503–12511. https://doi.org/10.1021/acs.analchem.8b02222.

(22) Richter, R. P.; Maury, N.; Brisson, A. R. On the Effect of the Solid Support on the Interleaflet Distribution of Lipids in Supported Lipid Bilayers. *Langmuir* **2005**, *21* (1), 299–304. https://doi.org/10.1021/la0478402.

(23) Jackman, J. A.; Ferhan, A. R.; Cho, N.-J. Surface-Based Nanoplasmonic Sensors for Biointerfacial Science Applications. *Bull. Chem. Soc. Jpn.* **2019**, *92* (8), 1404–1412. https://doi.org/10.1246/bcsj.20190112.

(24) van den Berg, A.; Bergveld, P.; Reinhoudt, D. N.; Sudhölter, E. J. Sensitivity Control of ISFETs by Chemical Surface Modification. *Sensors and Actuators* **1985**, *8* (2), 129–148. https://doi.org/https://doi.org/10.1016/0250-6874(85)87010-4.

(25) Sahai, N.; Sverjensky, D. A. Evaluation of Internally Consistent Parameters for the Triple-Layer Model by the Systematic Analysis of Oxide Surface Titration Data. *Geochim. Cosmochim. Acta* **1997**, *61* (14), 2801–2826.

https://doi.org/https://doi.org/10.1016/S0016-7037(97)00128-2.
(26) Galassi, C.; Bertoni, F.; Ardizzone, S.; Bianchi, C. L. Water-Based Si3N4 Suspensions: Part I. Effect of Processing Routes on the Surface Chemistry and Particle Interactions. *J. Mater. Res.* **2000**, *15* (1), 155–163. https://doi.org/DOI: 10.1557/JMR.2000.0026.
(27) Gersten, J. I.; Smith, F. W. *The Physics and Chemistry of Materials*; John Wiley & Sons, inc: New York, 2001.
(28) Ackler, H. D.; French, R. H.; Chiang, Y.-M. Comparisons of Hamaker Constants for Ceramic Systems with Intervening Vacuum or Water: From Force Laws and Physical Properties. *J. Colloid Interface Sci.* **1996**, *179* (2), 460–469. https://doi.org/https://doi.org/10.1006/jcis.1996.0238.
(29) Benesch, J.; Askendal, A.; Tengvall, P. Quantification of Adsorbed Human Serum Albumin at Solid Interfaces: A Comparison between Radioimmunoassay (RIA) and Simple Null Ellipsometry. *Colloids Surfaces B Biointerfaces* **2000**, *18* (2), 71–81. https://doi.org/https://doi.org/10.1016/S0927-7765(99)00136-8.
(30) Vörös, J.; Ramsden, J. J.; Csúcs, G.; Szendrő, I.; De Paul, S. M.; Textor, M.; Spencer, N. D. Optical Grating Coupler Biosensors. *Biomaterials* **2002**, *23* (17), 3699–3710. https://doi.org/https://doi.org/10.1016/S0142-9612(02)00103-5.
(31) Haes, A. J.; Chang, L.; Klein, W. L.; Van Duyne, R. P. Detection of a Biomarker for Alzheimer's Disease from Synthetic and Clinical Samples Using a Nanoscale Optical Biosensor. *J. Am. Chem. Soc.* **2005**, *127* (7), 2264–2271. https://doi.org/10.1021/ja044087q.
(32) McFarland, A. D.; Van Duyne, R. P. Single Silver Nanoparticles as Real-Time Optical Sensors with Zeptomole Sensitivity. *Nano Lett.* **2003**, *3* (8), 1057–1062. https://doi.org/10.1021/nl034372s.
(33) Zen, F.; Karanikolas, V. D.; Behan, J. A.; Andersson, J.; Ciapetti, G.; Bradley, A. L.; Colavita, P. E. Nanoplasmonic Sensing at the Carbon-Bio Interface: Study of Protein Adsorption at Graphitic and Hydrogenated Carbon Surfaces. *Langmuir* **2017**, *33* (17), 4198–4206. https://doi.org/10.1021/acs.langmuir.7b00612.
(34) Jonsson, M. P.; Jönsson, P.; Dahlin, A. B.; Höök, F. Supported Lipid Bilayer Formation and Lipid-Membrane-Mediated Biorecognition Reactions Studied with a New Nanoplasmonic Sensor Template. *Nano Lett.* **2007**, *7* (11), 3462–3468. https://doi.org/10.1021/nl072006t.
(35) Malmström, J.; Agheli, H.; Kingshott, P.; Sutherland, D. S. Viscoelastic Modeling of Highly Hydrated Laminin Layers at Homogeneous and Nanostructured Surfaces: Quantification of Protein Layer Properties Using QCM-D and SPR. *Langmuir* **2007**, *23* (19), 9760–9768. https://doi.org/10.1021/la701233y.
(36) Jackman, J. A.; Rahim Ferhan, A.; Cho, N.-J. Nanoplasmonic Sensors for Biointerfacial Science. *Chem. Soc. Rev.* **2017**, *46* (12), 3615–3660. https://doi.org/10.1039/C6CS00494F.
(37) Mazzotta, F.; Johnson, T. W.; Dahlin, A. B.; Shaver, J.; Oh, S.-H.; Höök, F. Influence of the Evanescent Field Decay Length on the Sensitivity of Plasmonic Nanodisks and Nanoholes. *ACS Photonics* **2015**, *2* (2), 256–262. https://doi.org/10.1021/ph500360d.
(38) Ferhan, A. R.; Jackman, J. A.; Cho, N.-J. Integration of Quartz Crystal Microbalance-Dissipation and Reflection-Mode Localized Surface Plasmon Resonance Sensors for Biomacromolecular Interaction Analysis. *Anal. Chem.* **2016**, *88* (24), 12524–12531. https://doi.org/10.1021/acs.analchem.6b04303.

(39) Estevez, M.-C.; Otte, M. A.; Sepulveda, B.; Lechuga, L. M. Trends and Challenges of Refractometric Nanoplasmonic Biosensors: A Review. *Anal. Chim. Acta* **2014**, *806*, 55–73. https://doi.org/https://doi.org/10.1016/j.aca.2013.10.048.

(40) Yonzon, C. R.; Jeoung, E.; Zou, S.; Schatz, G. C.; Mrksich, M.; Van Duyne, R. P. A Comparative Analysis of Localized and Propagating Surface Plasmon Resonance Sensors: The Binding of Concanavalin A to a Monosaccharide Functionalized Self-Assembled Monolayer. *J. Am. Chem. Soc.* **2004**, *126* (39), 12669–12676. https://doi.org/10.1021/ja047118q.

(41) Hutter, E.; Fendler, J. H. Exploitation of Localized Surface Plasmon Resonance. *Adv. Mater.* **2004**, *16* (19), 1685–1706. https://doi.org/10.1002/adma.200400271.

(42) Willets, K. A.; Van Duyne, R. P. Localized Surface Plasmon Resonance Spectroscopy and Sensing. *Annu. Rev. Phys. Chem.* **2007**, *58* (1), 267–297. https://doi.org/10.1146/annurev.physchem.58.032806.104607.

(43) Anker, J. N.; Hall, W. P.; Lyandres, O.; Shah, N. C.; Zhao, J.; Van Duyne, R. P. Biosensing with Plasmonic Nanosensors. *Nat. Mater.* **2008**, *7* (6), 442–453. https://doi.org/10.1038/nmat2162.

(44) Dahlin, A. B.; Wittenberg, N. J.; Höök, F.; Oh, S.-H. Promises and Challenges of Nanoplasmonic Devices for Refractometric Biosensing. *Nanophotonics 2* (2), 83–101. https://doi.org/https://doi.org/10.1515/nanoph-2012-0026.

(45) Nugroho, F. A. A.; Frost, R.; Antosiewicz, T. J.; Fritzsche, J.; Larsson Langhammer, E. M.; Langhammer, C. Topographically Flat Nanoplasmonic Sensor Chips for Biosensing and Materials Science. *ACS Sensors* **2017**, *2* (1), 119–127. https://doi.org/10.1021/acssensors.6b00612.

(46) Mensch, A. C.; Buchman, J. T.; Haynes, C. L.; Pedersen, J. A.; Hamers, R. J. Quaternary Amine-Terminated Quantum Dots Induce Structural Changes to Supported Lipid Bilayers. *Langmuir* **2018**, *34* (41), 12369–12378. https://doi.org/10.1021/acs.langmuir.8b02047.

(47) Tollefson, E. J.; Allen, C. R.; Chong, G.; Zhang, X.; Rozanov, N. D.; Bautista, A.; Cerda, J. J.; Pedersen, J. A.; Murphy, C. J.; Carlson, E. E.; et al. Preferential Binding of Cytochrome c to Anionic Ligand-Coated Gold Nanoparticles: A Complementary Computational and Experimental Approach. *ACS Nano* **2019**, *13* (6), 6856–6866. https://doi.org/10.1021/acsnano.9b01622.

(48) Cho, N.-J.; Frank, C. W.; Kasemo, B.; Höök, F. Quartz Crystal Microbalance with Dissipation Monitoring of Supported Lipid Bilayers on Various Substrates. *Nat. Protoc.* **2010**, *5* (6), 1096–1106. https://doi.org/10.1038/nprot.2010.65.

(49) Rodahl, M.; Höök, F.; Krozer, A.; Brzezinski, P.; Kasemo, B. Quartz Crystal Microbalance Setup for Frequency and Q-factor Measurements in Gaseous and Liquid Environments. *Rev. Sci. Instrum.* **1995**, *66* (7), 3924–3930. https://doi.org/10.1063/1.1145396.

(50) Reviakine, I.; Johannsmann, D.; Richter, R. P. Hearing What You Cannot See and Visualizing What You Hear: Interpreting Quartz Crystal Microbalance Data from Solvated Interfaces. *Anal. Chem.* **2011**, *83* (23), 8838–8848. https://doi.org/10.1021/ac201778h.

(51) Huang, R.; Yi, P.; Tang, Y. Probing the Interactions of Organic Molecules, Nanomaterials, and Microbes with Solid Surfaces Using Quartz Crystal Microbalances: Methodology, Advantages, and Limitations. *Environ. Sci. Process. Impacts* **2017**, *19* (6), 793–811. https://doi.org/10.1039/C6EM00628K.

(52) Sauerbrey, G. Verwendung von Schwingquarzen Zur Wägung Dünner Schichten Und Zur Mikrowägung. *Zeitschrift für Phys.* **1959**, *155* (2), 206–222. https://doi.org/10.1007/BF01337937.

(53) Johannsmann, D. Viscoelastic, Mechanical, and Dielectric Measurements on Complex Samples with the Quartz Crystal Microbalance. *Phys. Chem. Chem. Phys.* **2008**, *10* (31), 4516–4534. https://doi.org/10.1039/B803960G.

(54) Voinova, M. V; Rodahl, M.; Jonson, M.; Kasemo, B. Viscoelastic Acoustic Response of Layered Polymer Films at Fluid-Solid Interfaces: Continuum Mechanics Approach. *Phys. Scr.* **1999**, *59* (5), 391–396. https://doi.org/10.1238/physica.regular.059a00391.

(55) Keller, C. A.; Kasemo, B. Surface Specific Kinetics of Lipid Vesicle Adsorption Measured with a Quartz Crystal Microbalance. *Biophys. J.* **1998**, *75* (3), 1397–1402. https://doi.org/https://doi.org/10.1016/S0006-3495(98)74057-3.

(56) McGeachy, A. C.; Caudill, E. R.; Liang, D.; Cui, Q.; Pedersen, J. A.; Geiger, F. M. Counting Charges on Membrane-Bound Peptides. *Chem. Sci.* **2018**, *9* (18), 4285–4298. https://doi.org/10.1039/C8SC00804C.

(57) Gao, L.; Lemarchand, F.; Lequime, M. Refractive Index Determination of SiO2 Layer in the UV/Vis/NIR Range: Spectrophotometric Reverse Engineering on Single and Bi-Layer Designs. *J. Eur. Opt. Soc. - Rapid Publ. Vol 8* **2013**.

(58) McPeak, K. M.; Jayanti, S. V; Kress, S. J. P.; Meyer, S.; Iotti, S.; Rossinelli, A.; Norris, D. J. Plasmonic Films Can Easily Be Better: Rules and Recipes. *ACS Photonics* **2015**, *2* (3), 326–333. https://doi.org/10.1021/ph5004237.

(59) Philipp, H. R. Optical Properties of Silicon Nitride. *J. Electrochem. Soc.* **1973**, *120* (2), 295. https://doi.org/10.1149/1.2403440.

(60) Werner, C.; Körber, H.; Zimmermann, R.; Dukhin, S.; Jacobasch, H.-J. Extended Electrokinetic Characterization of Flat Solid Surfaces. *J. Colloid Interface Sci.* **1998**, *208* (1), 329–346. https://doi.org/https://doi.org/10.1006/jcis.1998.5787.

(61) Zimmermann, R.; Küttner, D.; Renner, L.; Kaufmann, M.; Zitzmann, J.; Müller, M.; Werner, C. Charging and Structure of Zwitterionic Supported Bilayer Lipid Membranes Studied by Streaming Current Measurements, Fluorescence Microscopy, and Attenuated Total Reflection Fourier Transform Infrared Spectroscopy. *Biointerphases* **2009**, *4* (1), 1–6. https://doi.org/10.1116/1.3082042.

(62) Zimmermann, R.; Küttner, D.; Renner, L.; Kaufmann, M.; Werner, C. Fluidity Modulation of Phospholipid Bilayers by Electrolyte Ions: Insights from Fluorescence Microscopy and Microslit Electrokinetic Experiments. *J. Phys. Chem. A* **2012**, *116* (25), 6519–6525. https://doi.org/10.1021/jp212364q.

(63) Hamblin, M. N.; Edwards, J. M.; Lee, M. L.; Woolley, A. T.; Hawkins, A. R. Electroosmotic Flow in Vapor Deposited Silicon Dioxide and Nitride Microchannels. *Biomicrofluidics* **2007**, *1* (3), 34101. https://doi.org/10.1063/1.2752376.

(64) Nishi, Y.; Doering, R.; Wooldrige, T. *Handbook of Semiconductor Manufacturing Technology*; 2000.

(65) Sundh, M.; Svedhem, S.; Sutherland, D. S. Formation of Supported Lipid Bilayers at Surfaces with Controlled Curvatures: Influence of Lipid Charge. *J. Phys. Chem. B* **2011**, *115* (24), 7838–7848. https://doi.org/10.1021/jp2025363.

(66) Weng, K. C.; Stålgren, J. J. R.; Duval, D. J.; Risbud, S. H.; Frank, C. W. Fluid Biomembranes Supported on Nanoporous Aerogel/Xerogel Substrates. *Langmuir* **2004**, *20* (17), 7232–7239. https://doi.org/10.1021/la049940d.

(67) Vishnyakov, A.; Li, T.; Neimark, A. V. Adhesion of Phospholipid Bilayers to Hydroxylated Silica: Existence of Nanometer-Thick Water Interlayers. *Langmuir* **2017**, *33* (45), 13148–13156. https://doi.org/10.1021/acs.langmuir.7b03582.

(68) Mitra, K.; Ubarretxena-Belandia, I.; Taguchi, T.; Warren, G.; Engelman, D. M. Modulation of the Bilayer Thickness of Exocytic Pathway Membranes by Membrane Proteins Rather than Cholesterol. *Proc. Natl. Acad. Sci.* **2004**, *101* (12), 4083 LP – 4088. https://doi.org/10.1073/pnas.0307332101.

(69) Renner, L. D.; Weibel, D. B. Cardiolipin Microdomains Localize to Negatively Curved Regions of <Em>Escherichia Coli</Em> Membranes. *Proc. Natl. Acad. Sci.* **2011**, *108* (15), 6264 LP – 6269. https://doi.org/10.1073/pnas.1015757108.

(70) De Feijter, J. A.; Benjamins, J.; Veer, F. A. Ellipsometry as a Tool to Study the Adsorption Behavior of Synthetic and Biopolymers at the Air–Water Interface. *Biopolymers* **1978**, *17* (7), 1759–1772. https://doi.org/10.1002/bip.1978.360170711.

(71) Reimhult, E.; Larsson, C.; Kasemo, B.; Höök, F. Simultaneous Surface Plasmon Resonance and Quartz Crystal Microbalance with Dissipation Monitoring Measurements of Biomolecular Adsorption Events Involving Structural Transformations and Variations in Coupled Water. *Anal. Chem.* **2004**, *76* (24), 7211–7220. https://doi.org/10.1021/ac0492970.

(72) Cuypers, P. A.; Corsel, J.; Janssen, M.; Kop, J. M. M.; Hermens, W.; Hemker, H. The Adsorption of Prothrombin to Phosphatidylserine Multilayers Quantitated by Ellipsometry. *J. Biol. Chem.* **1983**, *258*, 2426–2431.

Table of Contents Graphic